RSC Advances

PAPER

View Article Online
View Journal | View Issue

Cite this: *RSC Adv.*, 2025, **15**, 49488

Sustainable treatment and resource recovery from PCB acidic etching waste solution: Co-production technology of basic copper carbonate and copper oxide and transformation mechanisms

Song Ren,[a] Dengliang He,*[a] Shishan Xue,*[a] Shuxin Liu[a] and Wei Zhang[bc]

This study tackled the persistent challenges of low purity and limited diversity in recycled materials obtained from printed circuit board (PCB) acidic copper chloride etching waste solution (ACCEWS). High-purity $Cu_2(OH)_2CO_3$ was first synthesized from purified ACCEWS (in contrast to raw waste solutions) using a Na_2CO_3–$NaHCO_3$ buffer system. Subsequent alkaline treatment yielded crude CuO, which was then upgraded to high-purity CuO *via* calcination. Simultaneously, the effects of impurities on the purity, phase composition, and morphology of copper compounds were systematically investigated by XRD, SEM, TG, FTIR, ICP-OES, XPS and HRTEM, along with their transformation mechanisms and impurity behavior. The results demonstrated that purification markedly improved the purity of $Cu_2(OH)_2CO_3$. Compared to untreated samples, the P-$Cu_2(OH)_2CO_3$ derived from purified etching waste exhibited enhanced stability in copper content (55.40–55.50 wt% *vs.* 54.40–55.40 wt% in R-$Cu_2(OH)_2CO_3$), reduced metal impurities (0.17–0.22 wt%), and notably lower chloride residues (consistently ≤0.014 wt%). Furthermore, purification effectively removed competitive interference from Cl^- and other species during $Cu_2(OH)_2CO_3$ crystallization, yielding more uniform particles with either flower-like spherical or spiky flake morphologies. The combined purification and calcination process significantly improved both the purity and crystallization behavior of nano-CuO. The nano P-CuO showed progressively increasing CuO purity: 80.24 wt% (300 °C/1 h), 92.24 wt% (400 °C/1 h), 98.54 wt% (500 °C/1 h), and 98.80 wt% (600 °C/1 h) – consistently higher than that of the corresponding R-CuO samples derived from untreated waste (68.48 wt%, 82.24 wt%, 94.48 wt%, and 97.90 wt%). Final optimization at 600 °C for 3 hours yielded ultra-pure P-CuO nanoparticles (≈110 nm) containing 99.04 wt% CuO with exceptionally low impurity levels: <0.12 wt% metallic impurities and <0.0015 wt% chloride content. This study demonstrated a "waste-to-wealth" approach through the simultaneous production of high-purity $Cu_2(OH)_2CO_3$ and nano-CuO from the purification of ACCEWS. These findings offer important insights for both the sustainable utilization of PCB ACCEWS and the development of high-purity copper-based materials.

Received 23rd July 2025
Accepted 14th November 2025

DOI: 10.1039/d5ra05321h

rsc.li/rsc-advances

1. Introduction

In printed circuit board (PCB) manufacturing, chemical solutions (typically acidic copper chloride or alkaline ammonia) are used to dissolve unwanted copper layers from copper-clad laminates to create circuit patterns. This process generates copper ion-rich waste solutions, which are categorized into two main types: acidic etching waste and alkaline etching waste. The rapid advancement of the electronic information industry has significantly increased the global demand for PCBs in recent years.[1] The manufacturing of PCBs produces 1.5–3.5 liters of etching waste per square meter of board.[2] The annual volume of acidic and alkaline etching wastes has surpassed 10 billion cubic meters worldwide, with a growth rate of 15–18% per year,[3] while containing surpassing 70 000 metric tons of copper.[4] PCB etching solutions, as hazardous waste, contain elevated amounts of copper ions demonstrating bioaccumulation characteristics, which would present serious ecotoxicological hazards if released untreated.[5] Additionally, the exceptional copper grade within waste solution (typically >5% compared to 0.5–2% in natural ores) makes direct disposal economically wasteful and environmentally unsound.[6]

[a]*School of Chemistry and Material Engineering, Mianyang Teachers' College, Mianxing West Road No.166, Mianyang City, Sichuan Province, 621000, CN. E-mail: 449011902@qq.com; xueshishancarol@163.com*

[b]*Key Laboratory of Solid Waste Treatment and Resource Recycle, Ministry of Education, Mianyang City, Sichuan Province, 621000, CN*

[c]*Analytical and Testing Center, Southwest University of Science and Technology, Mianyang, 621000, CN*

Systematic copper recovery consequently would deliver valuable metal reclamation and crucial pollution prevention.

Currently, conventional approaches for PCB etching solution recycling comprise solvent extraction,[7] neutralization precipitation,[8] electrolysis,[9] and ion adsorption,[10] among others. For example, Nguyen *et al.* utilized Cyanex 272 to isolate Au(III) from a leaching solution of cemented Cu.[11] Liu *et al.*[12] proposed direct electrolysis to recover Cu from waste PCBs. The recovery rate of Cu was up to 97.32% with a purity of 99.86%.

These methods have demonstrated advantages in recovering precious metals, while the neutralization precipitation technique has garnered significant attention due to its straightforward process and low cost. Dou *et al.*[13] exploited an advanced approach of decomplexation and neutralization and precipitation by $NH_3 \cdot H_2O$ coupled with oxidation by O_2, to separate Cu(II) and Cu(I) to produce $Cu_2(OH)_3Cl$. Guo[14] and coworkers employed ammonia ($NH_3 \cdot H_2O$) and sodium hydroxide (NaOH) as neutralizers to reclaim Cu to produce $Cu_2Cl(OH)_3$, which can be used as a precursor for producing $Cu(OH)_2$ and $CuSO_4 \cdot 5H_2O$ with higher purity.

Basic copper carbonate (BCC; $Cu_2(OH)_2CO_3$), another normal copper-containing compound, can also be fabricated through neutralization precipitation, which has been widely applied in various fields including pyrotechnics, pigments, insecticides, organic synthesis catalysts, and others.[15–20] A typical process involved either reacting metallic copper with concentrated HNO_3 to prepare $Cu(NO_3)_2$ or directly using $Cu(NO_3)_2$ as the raw material, with ammonium bicarbonate serving as the precipitating agent to afford $Cu_2(OH)_2CO_3$.[21] Alternative approaches have been reported, such as directly precipitating $Cu_2(OH)_2CO_3$ crystals (5.0–6.5 μm) from a $CuCl_2$ solution and Na_2CO_3 solution at 50 °C and pH 6.5–9.[22] Additionally, Candal *et al.*[23] employed a copper-containing solution with ammonia water as a pH regulator to prepare amorphous $Cu_2(OH)_2CO_3$.

Despite BCC being widely applied in many fields, the economic efficiency is hardly attractive. However, BCC always works as a precursor to produce CuO, for which the high specific capacity, surface energy, and large surface area lead to promising applications in advanced fields, including electrochemical devices, optoelectronics, energy systems, catalysis, and biomedicine. The fabrication of CuO nanoparticles is generally achieved through physical, chemical, and biogenic techniques. Chemical precipitation combined with thermal decomposition is one of the most simple, low-cost and scalable techniques to produce CuO. Luna *et al.*[24] synthesized CuO using cupric acetate as a precursor at 400 °C for 1 h under an air flow. Benhammada *et al.*[25] utilized nitrate trihydrate, copper(II) chloride dehydrate, and copper(II) sulfate pentahydrate as precursors, respectively, which were further precipitated by NaOH solution. The obtained precipitates were annealed at 550 °C for 4 h to produce CuO. Kida *et al.*[26] developed 5–10 nm CuO-NPs *via* ethanol-based solution-phase synthesis at 78 °C using $Cu(CH_3COO)_2$ in a CH_3COOH/NaOH system. Chang *et al.*[27] produced 40–50 nm CuO-NPs through 500 °C calcination of $CuSO_4/Na_2CO_3$ precursors. Gan *et al.*[28] achieved 20 nm crystalline CuO-NPs *via* chloride-based precipitation with ultrasonic purification.

Inspired by these published works, herein, we propose a coupling technique of neutralization precipitation and thermal decomposition to fabricate high-purity CuO using acidic copper chloride etching waste solutions (ACCEWS) as copper sources. The production technology of $Cu_2(OH)_2CO_3$ was studied in detail, including the $Na_2CO_3/NaHCO_3$ ratio and reaction temperature during the neutralization precipitation process. The low-temperature hydrothermal conversion and calcination parameters were also researched in depth to synthesize CuO. The as-prepared CuO obtained using the optimal parameters exhibited high purity (>99.04 wt%), low metallic impurities (<0.12 wt%) and low chloride content (<0.0015 wt%). This innovative strategy resolved the single-product constraint of traditional recovery processes, accomplishing coupled production of two valuable copper compounds and establishing an efficient hazardous waste upcycling paradigm.

2. Results and discussion

2.1 Preparation of high-purity $Cu_2(OH)_2CO_3$ and its influence mechanisms

In this section, the copper purity, impurity contents, crystalline phase and particle morphology of $Cu_2(OH)_2CO_3$ prepared by R-ACCEWS and P-ACCEWS are systematically investigated, determining the relationships between these properties and experimental parameters, including purification pretreatment, alkali ratio ($Na_2CO_3/NaHCO_3$), and reaction temperature.

2.1.1 The influence of $Na_2CO_3/NaHCO_3$ ratio. XRD was employed to characterize the crystal structure of $Cu_2(OH)_2CO_3$ prepared from P-ACCEWS at different $Na_2CO_3/NaHCO_3$ ratios (1 : 2, 1 : 1, 2 : 1). As shown in Fig. 1A, all the products displayed well-defined diffraction peaks at 14.8°, 17.6°, 24.1°, and 31.2°, precisely corresponding to the (020), (120), (220), and (20–1) crystal planes of monoclinic $Cu_2(OH)_2CO_3$ (JCPDS no. 41-1390), respectively, indicating their high crystallinity. The XRD patterns confirmed that P-ACCEWS consistently produced well-crystallized, high-purity $Cu_2(OH)_2CO_3$ across different alkali ratios. This enhanced crystallization was mainly due to the effective elimination of interfering impurities (*e.g.*, Cl^- and metal ions), which created an optimized growth environment for monoclinic $Cu_2(OH)_2CO_3$ crystals. In contrast, the products derived from R-ACCEWS at a 1 : 1 $Na_2CO_3/NaHCO_3$ ratio exhibited monoclinic $CuCl(OH)_3$ (JCPDS no. 87-0679) as the dominant phase, suggesting that competitive coordination of chloride suppressed the formation of $Cu_2(OH)_2CO_3$ at low alkalinity. At a 1 : 2 $Na_2CO_3/NaHCO_3$ ratio, monoclinic $Cu_2(OH)_2CO_3$ from R-ACCEWS became the major phase. However, an unidentified impurity peak emerged at 22.2°, likely due to metallic impurity compounds. When the $Na_2CO_3/NaHCO_3$ ratio was further increased to 2 : 1, monoclinic $Cu_2(OH)_2CO_3$ formed as the exclusive phase, demonstrating that higher CO_3^{2-}/OH^- concentrations effectively overcame the interference from chloride.

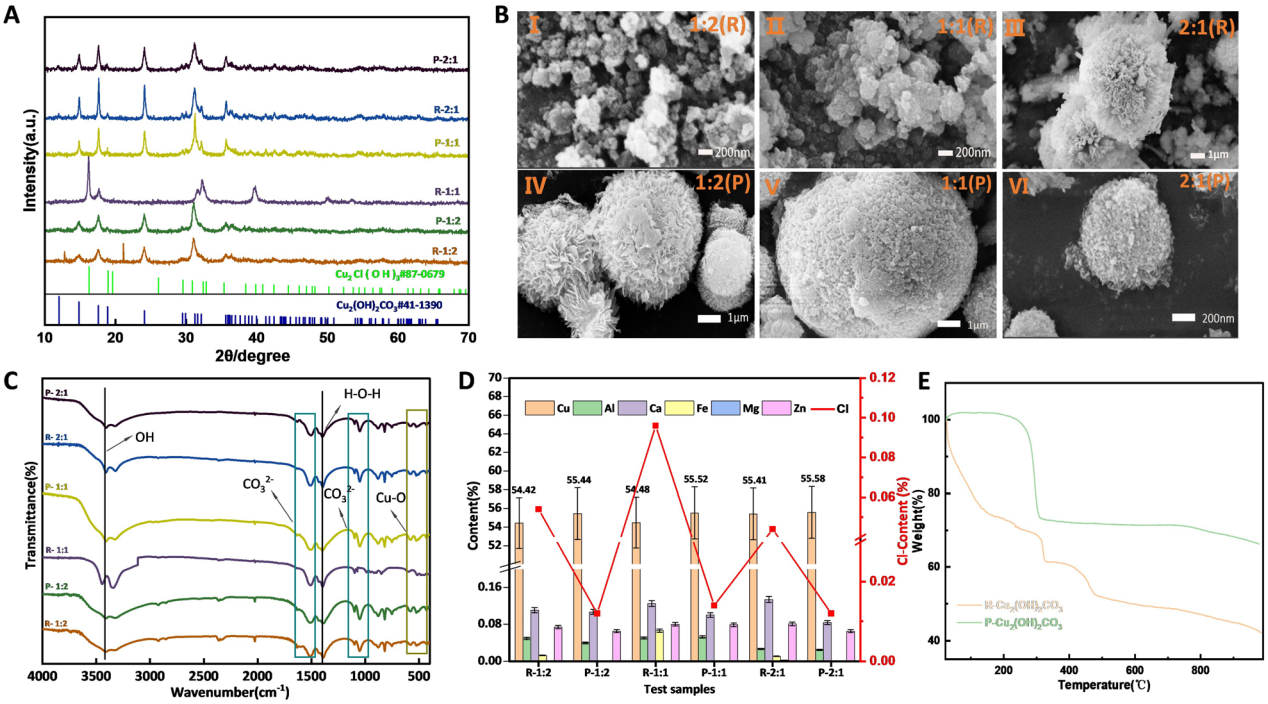

Fig. 1 (A) XRD patterns, (B) SEM images, and (C) FTIR spectra of $Cu_2(OH)_2CO_3$. (D) The Cu contents and impurity contents in $Cu_2(OH)_2CO_3$ obtained at different alkali ratios. (E) The TGA curves of R-$Cu_2(OH)_2CO_3$ and P-$Cu_2(OH)_2CO_3$.

It was found that the morphology and dispersity of $Cu_2(OH)_2CO_3$ were significantly influenced by the type of ACCEWS. Compared to $Cu_2(OH)_2CO_3$ obtained from R-ACCEWS, $Cu_2(OH)_2CO_3$ derived from P-ACCEWS exhibited superior dispersity and more regular morphology (Fig. 1B). Additionally, the alkali ratio of Na_2CO_3/$NaHCO_3$ also affected the morphology of $Cu_2(OH)_2CO_3$. In the R-ACCEWS system, increasing the Na_2CO_3 ratio caused R-$Cu_2(OH)_2CO_3$ to evolve from irregular fine particles (~40 nm) with severe agglomeration at 1 : 2 and 1 : 1 Na_2CO_3/$NaHCO_3$ ratios to irregular flaky particles forming 5–6 μm flower-like clusters at 2 : 1 Na_2CO_3/$NaHCO_3$. By contrast, the P-ACCEWS system showed distinctly different morphological evolution: well-dispersed 6–8 μm flaky particle clusters formed at a 1 : 2 Na_2CO_3/$NaHCO_3$ ratio, transforming into densely packed ~10 μm spherical aggregates at a 1 : 1 Na_2CO_3/$NaHCO_3$ ratio, and finally yielding mixed spherical/thorny-flake morphologies (~1 μm) at a 2 : 1 Na_2CO_3/$NaHCO_3$ ratio. The findings confirmed that purification successfully eliminated etching solution-derived impurities, which was critical for achieving controlled nucleation and subsequent growth of $Cu_2(OH)_2CO_3$ crystals (Fig. 1B).

The functional groups of $Cu_2(OH)_2CO_3$ were investigated by FTIR. The characteristic absorption peaks at 460 cm^{-1} and 530 cm^{-1} assigned to Cu–O stretching vibrations are observed in Fig. 1C. Additionally, the spectral features observed at 1100 cm^{-1} and 1550 cm^{-1} were attributed to the symmetric and asymmetric stretching modes of carbonate (CO_3^{2-}) groups, respectively. Comparative FTIR spectra demonstrated that the purification process substantially influenced the characteristic infrared absorption profiles of the synthesized products. The characteristic CO_3^{2-} vibration modes at 1100 cm^{-1} and 1550 cm^{-1} exhibited significantly greater intensity for R-$Cu_2(OH)_2CO_3$. This enhancement likely originated from carbonate impurities derived from metal ion leaching in the R-ACCEWS system during precipitation. Subsequent purification effectively eliminated these interfering ionic species, resulting in phase-pure $Cu_2(OH)_2CO_3$. The variation in the Na_2CO_3 ratio notably influenced the hydroxyl group vibrational characteristics. With the Na_2CO_3 ratio increasing, all samples exhibited enhanced –OH peak intensities near 3400 cm^{-1}, particularly prominent for P-$Cu_2(OH)_2CO_3$ and R-$Cu_2(OH)_2CO_3$ samples at a 1 : 1 Na_2CO_3/$NaHCO_3$ ratio. These spectroscopic changes indicated that alkalinity facilitates $Cu_2(OH)_2CO_3$ crystallization, while simultaneously enhancing hydrogen-bonding networks through increased hydroxyl group density in the precipitated phases.

As shown in Fig. 1D, R-$Cu_2(OH)_2CO_3$ contained 54.40 wt%, 54.48 wt%, and 55.40 wt% copper for Na_2CO_3/$NaHCO_3$ ratios of 1 : 2, 1 : 1, and 2 : 1 respectively, with corresponding metallic impurity contents of 0.26 wt%, 0.24 wt%, and 0.27 wt%, and chloride contents of 0.044 wt%, 0.090 wt%, and 0.042 wt%, respectively. In comparison, P-$Cu_2(OH)_2CO_3$ from P-ACCEWS demonstrated copper contents of 55.40 wt%, 55.50 wt%, and 55.40 wt% at the same Na_2CO_3/$NaHCO_3$ ratios, with metallic impurities measuring 0.21 wt%, 0.22 wt%, and 0.17 wt%, and chloride contents of 0.012 wt%, 0.014 wt% and 0.012 wt% respectively. The experimental results demonstrated that the purification treatment significantly improved the purity of $Cu_2(OH)_2CO_3$. The copper content in P-$Cu_2(OH)_2CO_3$ (55.40–55.50%) showed better consistency across different Na_2CO_3/$NaHCO_3$ ratios and closer approximation to the theoretical

value (55.42 wt%) compared to R-$Cu_2(OH)_2CO_3$ (54.40–55.40 wt%). Furthermore, purification effectively reduced metallic impurities (0.17–0.22 wt% in P-$Cu_2(OH)_2CO_3$ *versus* 0.24–0.27 wt% in R-$Cu_2(OH)_2CO_3$) and substantially suppressed chloride residues (all ≤0.014 wt% in P-$Cu_2(OH)_2CO_3$, with certain batches showing over 50 wt% reduction). Notably, iron content fell below the detection limit after purification, indicating particularly outstanding removal efficiency for specific metals. When evaluated against Chinese industrial standards for BBC, the copper content and chloride levels for P-$Cu_2(OH)_2CO_3$ satisfied Class I product requirements, while Fe, Pb, Zn, Cr, Cd, and As contents complied with Class II standards. In contrast, the products prepared from R-ACCEWS contained excessive metallic impurities and failed to meet standard requirements.

The thermal behavior of as-prepared $Cu_2(OH)_2CO_3$ was investigated by TGA in this work (Fig. 1E). The TGA curve of R-$Cu_2(OH)_2CO_3$ exhibited multiple weight loss steps between 30 and 450 °C with a total weight loss of 48% attributed to the decomposition of $Cu_2(OH)_2CO_3$ (eqn (1) and (2)) and impurities (eqn (4) and (5)). An additional 10% weight loss occurred between 480 and 980 °C, probably resulting from further decomposition of $Cu_2(OH)_2CO_3$ (eqn (3)) and impurities with hydroxyl and carbonate groups. In contrast, the TGA curve of P-$Cu_2(OH)_2CO_3$ displayed only one distinct weight loss step (25%) in the 30–320 °C range, mainly due to $Cu_2(OH)_2CO_3$ decomposition (eqn (1) and (2)), followed by a gradual 9% weight loss between 400 and 1000 °C that may be caused by eqn (3).[29,30]

$$2\left[Cu_2(OH)_2CO_3\right] \xrightarrow{95-250\ ^\circ C} 2CuCO_3\cdot Cu(OH)_2 + H_2O + CuO \quad (1)$$

$$2CuCO_3\cdot Cu(OH)_2 \xrightarrow{310-450\ ^\circ C} 2CuO + Cu(OH)_2 + 2CO_2\uparrow \quad (2)$$

$$Cu(OH)_2 \xrightarrow{450-850\ ^\circ C} CuO + H_2O \quad (3)$$

The analytical results demonstrated that the purification pretreatment effectively removed Cl^- and other impurities from the etching solution, thereby eliminating competitive interference during $Cu_2(OH)_2CO_3$ crystallization and enabling consistent production of phase-pure, highly crystalline $Cu_2(OH)_2CO_3$ across all Na_2CO_3/$NaHCO_3$ ratios. The reduced impurity content promoted regular crystal growth, yielding better particle dispersion and more uniform morphologies (*e.g.*, spherical clusters or thorny flakes), along with copper content substantially closer to theoretical values and fewer metallic impurities.

2.1.2 The influence of reaction temperature. The synthesis of $Cu_2(OH)_2CO_3$ was carried out using P-ACCEWS (Na_2CO_3/$NaHCO_3$ ratio = 1 : 1) according to the process flow in Scheme 1, with reaction temperatures systematically varied at 50 °C, 70 °C, and 90 °C. As shown in Fig. 2A, temperature-dependent color evolution was observed: the 50 °C product formed fine blue powders, whereas both 70 °C and 90 °C conditions yielded distinct emerald-green particulate products. The SEM images (Fig. 2B) clearly revealed a significant morphological transition correlated with synthesis temperature: products obtained at 50 °C display uniformly shaped prismatic rods with well-developed facets (20–40 μm in length), contrasting sharply with the 70 °C product's nanostructure-assembled spherical secondary particles (approximately 10 μm in diameter). Most remarkably, elevated temperature (90 °C) processing led to the formation of defective spherical aggregates showing pronounced structural fragmentation.

Moreover, the precipitates obtained at 50 °C showed main diffraction peaks at 13.8°, 23.8°, 25.1°, 22.4°, 28.7° and 29.0°, corresponding to monoclinic $Na_2Cu(CO_3)_2(H_2O)_3$ phase (JCPDS no. 87-0679) (Fig. 2C). In contrast, precipitates obtained at 70 °C and 90 °C displayed characteristic peaks at 14.8°, 17.6°, 25.1° and 31.2°, matching the monoclinic $Cu_2(OH)_2CO_3$ phase (JCPDS no. 41-1390). These results illustrated that the reaction temperature significantly influenced both the phase composition and morphology of the products.

FTIR spectra of precipitates obtained at different temperatures showed characteristic peak variations with increasing temperature from 50 °C to 90 °C (Fig. 2D). The peaks at 3400 cm^{-1}, 477–530 cm^{-1} and 1600 cm^{-1} assigned to –OH stretching vibration, Cu–O stretching vibration and CO_3^{2-} absorption, respectively, were observed to be apparently enhanced, indicating complete conversion to $Cu_2(OH)_2CO_3$ with increased intermolecular bonding. The spectral shift of coordinated CO_3^{2-} asymmetric stretching (from 1550–1510 cm^{-1} to 1450–1500 cm^{-1}) confirmed this structural evolution. Interestingly, the 70 °C products showed stronger CO_3^{2-} signals than the 90 °C sample, suggesting temperature-induced morphological changes (particle fracturing) reduced functional group availability, this being consistent with the SEM results.

Fig. 2E demonstrates the temperature-dependent variations in copper content, metallic impurities, and chloride level of the synthesized products. Notably, the 50 °C product showed markedly reduced copper content (40.40 wt%, primarily $Na_2Cu(CO_3)_2(H_2O)_3$ phase) compared to the 70 °C (55.44%) and 90 °C (55.48 wt%) products. Importantly, all synthesized products maintained chloride concentrations <0.015 wt% and acceptable metal impurity levels, validating the purification process's effectiveness. The characterization (XRD, SEM, FTIR and elemental analysis) conclusively established reaction temperature as the critical parameter governing both crystalline phase and morphological features. Optimal synthesis of phase-pure, morphologically uniform $Cu_2(OH)_2CO_3$ required precise temperature regulation at 70 °C.

2.2 Low-temperature hydrothermal conversion-calcination synthesis of high-purity CuO from $Cu_2(OH)_2CO_3$

High-purity CuO was synthesized *via* low-temperature hydrothermal conversion-calcination from $Cu_2(OH)_2CO_3$ (prepared as described in Section 3.1) as the precursor. In this section, our team systematically researched the influence of technological conditions, including reaction temperature and time, on the products' CuO contents, impurity levels, phase compositions, and morphological characteristics.

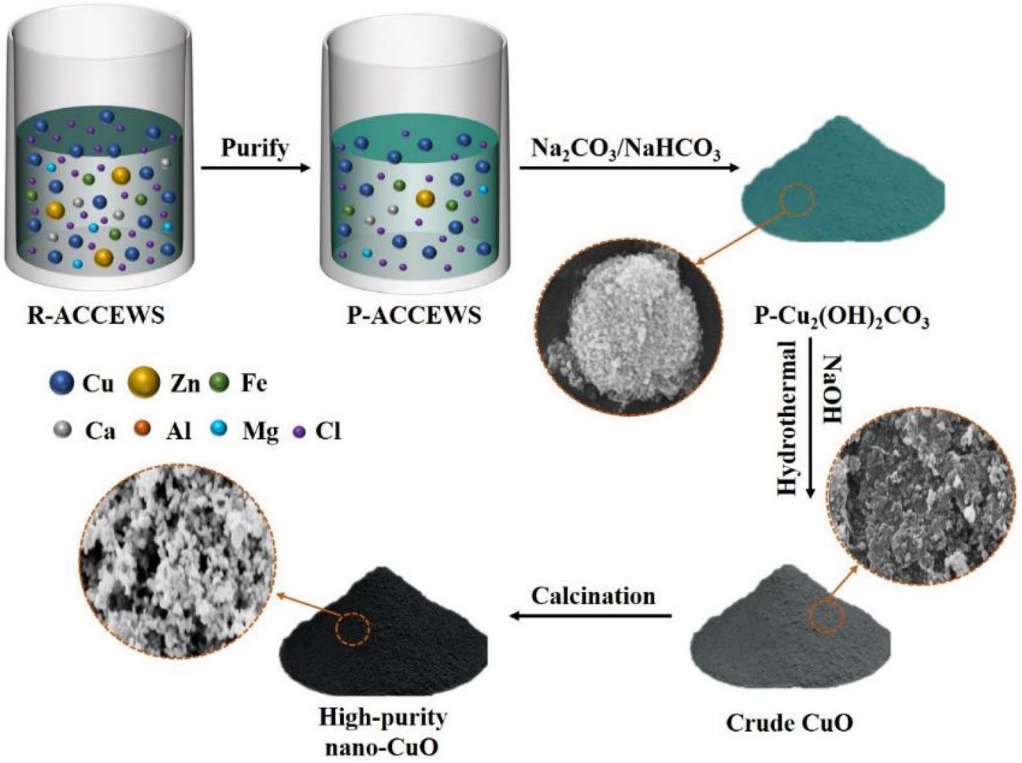

Scheme 1 Illustration of the transformation mechanisms of Cu within ACCEWS.

2.2.1 CuO obtained *via* low-temperature hydrothermal conversion from $Cu_2(OH)_2CO_3$. XRD patterns of crude P-CuO (derived from P-ACCEWS) and crude R-CuO (derived from R-ACCEWS) are displayed in Fig. 3A, both synthesized using $Cu_2(OH)_2CO_3$ as the precursor at a Na_2CO_3/$NaHCO_3$ ratio of 2 : 1. Crude R-CuO exhibited main diffraction peaks at 14.8°, 16.1°, 17.5°, 24.0°, 31°, 32.5°, 32.6°, 35.5°, and 35.9°. According to the Powder Diffraction Database, the main characteristic peaks of rhombohedral $Cu_2Cl(OH)_3$ appeared at 16.1° (011) and 17.6° (101), while monoclinic $Cu_2(OH)_2CO_3$ showed primary peaks at 14.7° (020), 24.0° (220), and 31.3° (20–1). The diffraction peaks of monoclinic CuO were at 32.6° (110), 35.4° (−111), and 38.8° (111). The phase composition analysis conducted using Jade 9.0 software confirmed the presence of three predominant crystalline phases in crude R-CuO: rhombohedral $Cu_2Cl(OH)_3$ (JCPDS no. 78-0372), monoclinic $Cu_2(OH)_2CO_3$ (JCPDS no. 41-1390), and monoclinic CuO (JCPDS no. 89-5897).

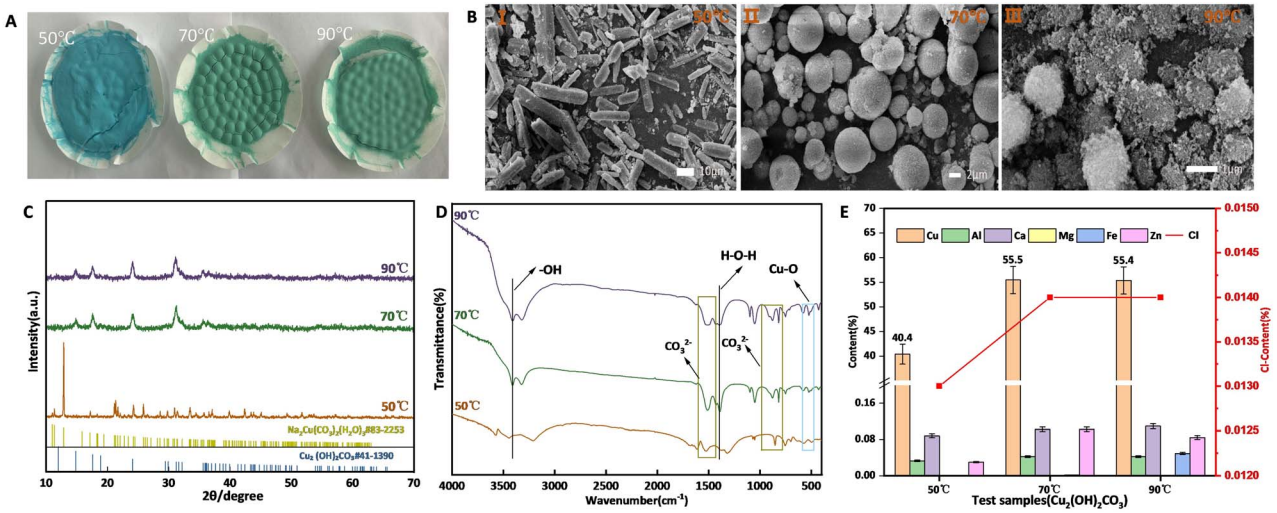

Fig. 2 (A) Digital photograph, (B) SEM images, (C) XRD patterns, and (D) FTIR spectra of $Cu_2(OH)_2CO_3$. (E) Cu contents and impurity contents of $Cu_2(OH)_2CO_3$ obtained at different temperatures.

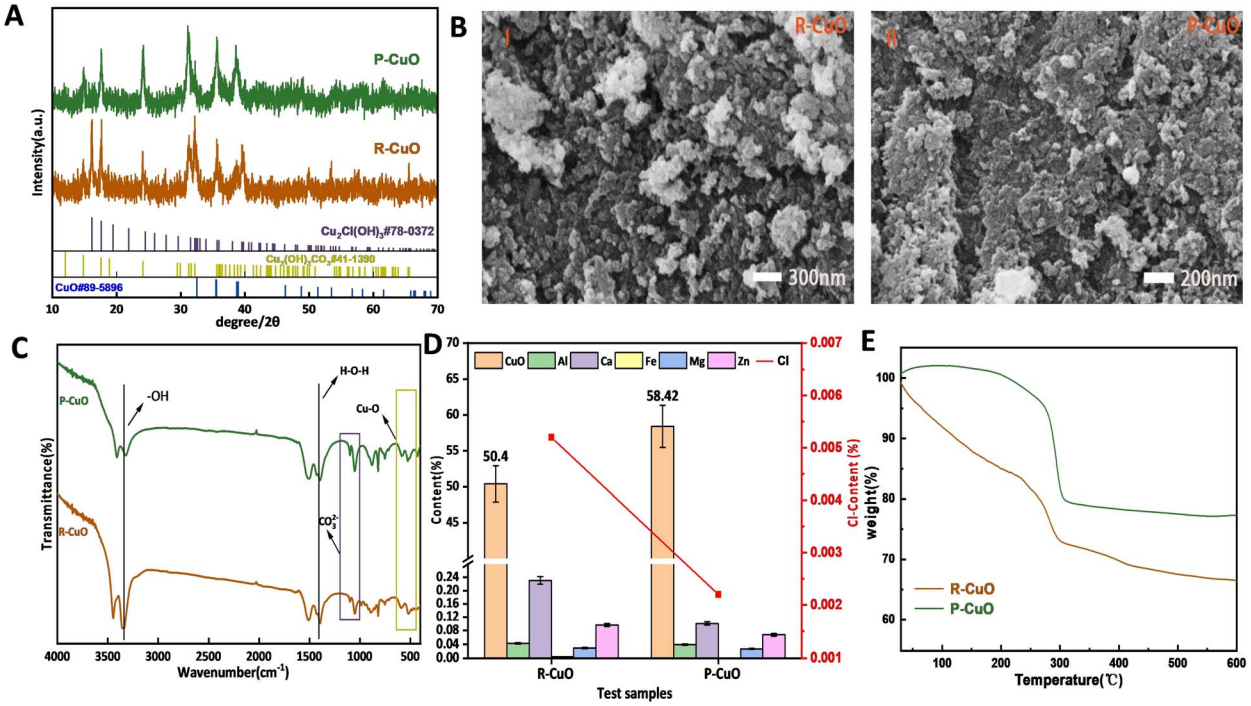

Fig. 3 (A) XRD patterns; (B) SEM images; (C) FTIR spectra; (D) CuO contents and impurity contents; (E) TGA curves of R-CuO and P-CuO.

The primary phases identified in crude P-CuO include monoclinic $Cu_2(OH)_2CO_3$ (JCPDS no. 41-1390), monoclinic CuO (JCPDS no. 89-5897), and rhombohedral $Cu_2Cl(OH)_3$ (JCPDS no. 78-0372), with characteristic diffraction peaks observed at 12.4°, 14.8°, 16.1°, 17.5°, 24.0°, 31.5°, 32.5°, 32.6°, 35.5°, and 35.9°. Notably, the peak intensities of crude P-CuO at 16.1° (011) and 17.5° (101), corresponding to $Cu_2Cl(OH)_3$, were significantly weaker compared to those of crude R-CuO, indicating a substantial reduction in $Cu_2Cl(OH)_3$ content in crude P-CuO.

The XRD patterns demonstrated that CuO constitutes the dominant phase in both R-CuO and P-CuO, accounting for approximately 60% of the total diffraction peak intensity. The presence of $Cu_2Cl(OH)_3$ impurities originated from chloride ions (Cl^-) in the raw etching solutions, whose complexation with Cu^{2+} ions inhibited complete hydrolysis. However, the purification effectively reduced the $Cu_2Cl(OH)_3$ content in crude P-CuO. The presence of residual $Cu_2(OH)_2CO_3$ indicated incomplete precursor decomposition, caused by an insufficient hydrothermal temperature (95 °C).

The crude P-CuO and R-CuO exhibited significant particle agglomeration (30–40 nm) (Fig. 3B), ascribed to the 95 °C hydrothermal reaction temperature, which favors smaller nanoparticle formation. Additionally, incomplete decomposition of $Cu_2(OH)_2CO_3$ during the process might result in residual CO_3^{2-} or OH^- adsorbed on particle surfaces. These species could form bridging bonds (*e.g.*, Cu–O–CO_3–Cu), thereby connecting individual particles into aggregates.

FTIR spectra demonstrated that crude P-CuO exhibited stronger absorption peaks at 1110 cm^{-1} (CO_3^{2-}) and 530 cm^{-1} (Cu–O), possibly due to its higher crystallinity and larger particle size leading to more incomplete thermal decomposition, which enhanced the vibrational signals of Cu–O bonds and CO_3^{2-} groups (Fig. 3C). In contrast, crude R-CuO showed significantly weaker signals near 3400 cm^{-1} (–OH) and 1400 cm^{-1} (H–O–H), possibly caused by its higher content of hydroxyl impurities.

Furthermore, crude R-CuO contained 50.4 wt% CuO, with 0.42 wt% metallic impurities and 0.0052 wt% chloride. In comparison, crude P-CuO demonstrated significantly improved purity with 58.42 wt% CuO content, along with reduced metallic impurities (0.23 wt%) and lower chloride content (0.0022 wt%) (Fig. 3D). These results confirmed that the purification treatment effectively enhanced the CuO content while simultaneously decreasing both metallic and chloride impurity levels in the crude CuO.

The TGA curves of crude R-CuO and P-CuO showed distinct differences (Fig. 3E). For crude R-CuO, the weight loss was 15% at 30–240 °C, 10% at 240–300 °C, 8% at 300–450 °C, and 4% at 450–600 °C, with a total weight loss of 37%. In comparison, crude P-CuO exhibited weight losses of 2% (30–230 °C), 4% (230–270 °C), 15% (270–300 °C), and 2% (300–600 °C), resulting in a significantly lower total weight loss of 23%. The thermogravimetric results confirmed the significant differences in thermal behavior between crude R-CuO and crude P-CuO. Crude P-CuO exhibited only a 3% weight loss in the 30–230 °C range, primarily attributed to adsorbed water removal, whereas crude R-CuO showed substantially higher weight loss (15%) due to combined water desorption and thermal decomposition of impurity compounds (Fe, Ca) (eqn (1), (4) and (6)).[31] The subsequent weight losses of crude P-CuO at 230–270 °C and 270–300 °C correspond to the decomposition of $Cu_2(OH)_2CO_3$ (eqn (1) and (2)) and $Cu(OH)_2$ pyrolysis (eqn (3)), respectively,

with a total weight loss of 23% – markedly lower than crude R-CuO weight loss of 34%. This discrepancy confirmed that crude P-CuO contains significantly reduced chloride and impurity content, as evidenced by the absence of substantial weight loss contributions from $Cu_2Cl(OH)_3$ decomposition (eqn (7) and (8)) that account for 22% of crude R-CuO's total weight loss between 240 and 600 °C. Ultimately, crude P-CuO achieves higher CuO content (58.42% *vs.* 50.4% in crude R-CuO), validating that purification effectively removed Fe/Ca impurities and chlorides, minimized thermal decomposition losses, and enhanced both product purity and effective CuO yield.

$$Fe_2(CO_3)_3\cdot xFe(OH)_3\cdot yH_2O \xrightarrow{30-200\ ^\circ C} Fe_2(CO_3)_3\cdot xFe(OH)_3 + yH_2O \quad (4)$$

$$Fe_2(CO_3)_3 \xrightarrow{300-500\ ^\circ C} Fe_2O_3 + 3CO_2\uparrow \quad (5)$$

$$CaCO_3\cdot xCa(OH)_2\cdot yH_2O \xrightarrow{30-900\ ^\circ C} (x+1)CaCO_3 + (y+x)H_2O \quad (6)$$

$$6Cu_2Cl(OH)_3 \xrightarrow{200-350\ ^\circ C} CuCl_2 + 2CuCl + 9H_2O + 9CuO + Cl_2\uparrow \quad (7)$$

$$4CuCl + 2CuCl_2 + 3O_2 \xrightarrow{500-600\ ^\circ C} 6CuO + 4Cl_2\uparrow \quad (8)$$

2.2.2 High-purity CuO obtained *via* calcination technology from crude CuO

2.2.2.1 Calcination temperature. High-purity CuO was prepared by calcination at 300 °C, 400 °C, 500 °C, and 600 °C using crude P-CuO and R-CuO as raw materials. XRD results indicated that the main diffraction peaks of the calcined R-CuO and P-CuO appeared at 32.4° (110), 35.3° (−111), 38.5° (111), 48.8° (−202), 53.3° (020), 58.1° (202), 61.5° (−113), 66.2° (−311), and 67.9° (220) (Fig. 4A). Phase analysis using Jade 9.0 software confirmed the predominant presence of monoclinic CuO (JCPDS no. 89-5897) in both R-CuO and P-CuO calcined products. Furthermore, calcination temperature significantly influenced the phase composition and crystallinity of the products, indicated by the XRD patterns shown in Fig. 4A. While both crude R-CuO and crude P-CuO precursors may form CuO crystals during 300 °C calcination, R-CuO exhibited slightly weaker diffraction intensities along with an impurity peak at 16.1° corresponding to rhombohedral $Cu_2Cl(OH)_3$ (JCPDS no. 78-0372), indicating incomplete removal of this impurity at 300 °C. Upon increasing the temperature to 400 °C, the $Cu_2Cl(OH)_3$ peaks disappeared in the patterns of both R-CuO and P-CuO and sharper diffraction peaks appeared; further crystallinity enhancement occurred at 600 °C. Notably, both R-CuO and P-CuO demonstrated preferential growth along the (110, 21.4°), (−111, 35.5°), (111, 38.8°), (200, 38.9°), and (−202, 48.7°) crystal planes.

As shown in Fig. 4B, both R-CuO (300 °C) and R-CuO (400 °C) consisted of irregularly shaped fine particles. The particle size of R-CuO (500 °C) was approximately 100 nm with severe agglomeration, while R-CuO (600 °C) displayed particles of around 110 nm in size, accompanied by significant particle aggregation. In contrast, P-CuO (300 °C) presented well-defined nanoparticles. P-CuO (400 °C) clearly displayed porous structures, forming aggregated morphologies composed of sheet-like, needle-like, and fine particulate components. Both P-CuO (500 °C) and P-CuO (600 °C) demonstrated regular morphologies with uniform particle sizes ranging from 110 to 120 nm.

The morphological differences between R-CuO and P-CuO reflected the crucial influence of precursor composition and calcination temperature on crystallization behavior and particle growth kinetics.[32] In the R-CuO series, both 300 °C and 400 °C calcined products consisted of irregular fine particles without

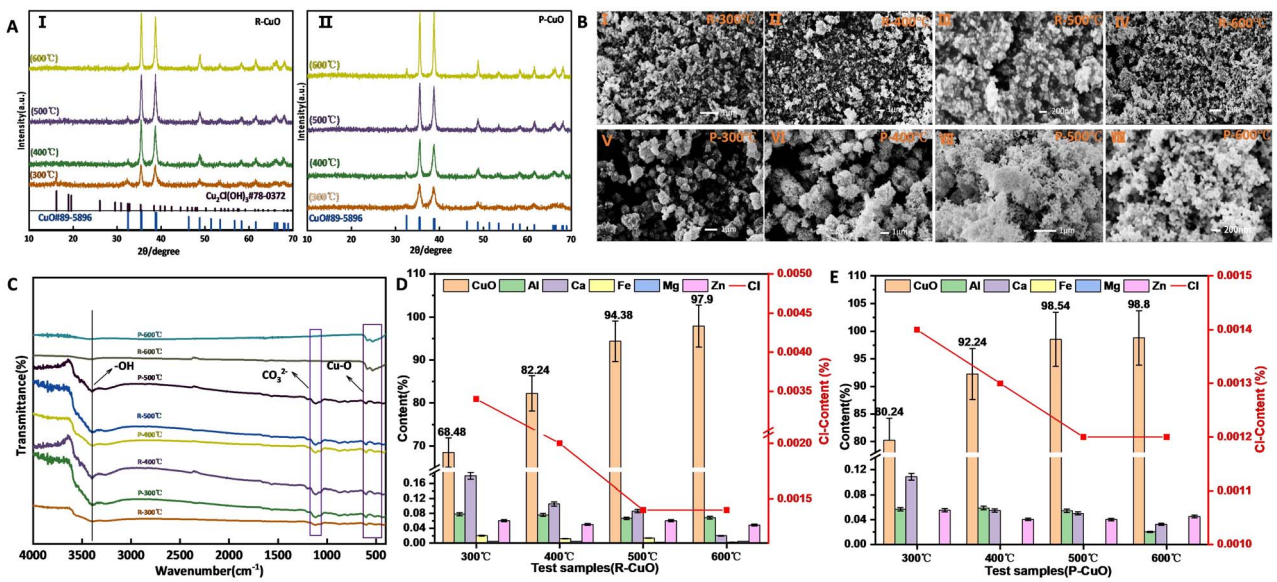

Fig. 4 (A) XRD patterns, (B) SEM images, and (C) FTIR spectra of products calcined at different temperatures. CuO contents and impurity contents of (D) R-CuO and (E) P-CuO.

significant morphological differences, indicating weak temperature effects on nucleation processes below 400 °C. When the temperature increased to 500 °C, the particle size grew to approximately 100 nm with severe agglomeration. In contrast, the P-CuO series exhibited distinct growth characteristics. Obviously, the 300 °C product formed extremely small-sized particles, while at 400 °C, distinct pore structures appeared along with complex aggregates composed of sheet-like, needle-like, and fine particulate morphologies. When the temperature reached 500–600 °C, the products transformed into uniform nanoparticles (110–120 nm) with well-defined shapes, suggesting that the purified precursor favors the formation of size-controlled nanostructures at high temperatures. This divergence likely originated from altered thermal decomposition pathways due to impurity removal during the etching purification process, which subsequently modified the anisotropic growth behavior of CuO crystals.

As shown in Fig. 4C, all CuO calcined below 500 °C exhibited –OH stretching (3400 cm^{-1}) and bending (1600 cm^{-1}) peaks, indicating incomplete decomposition of $Cu(OH)_2$. When the temperature rose to 600 °C, the –OH peaks weakened significantly, showing complete hydroxyl removal and formation of a perfect CuO crystal structure. Meanwhile, the Cu–O characteristic peaks at 460–530 cm^{-1} become sharper and stronger with increasing temperature, illustrating CuO grain growth and improved crystallinity. Additionally, all products below 500 °C showed a CO_3^{2-} peak near 1200 cm^{-1} from residual $Cu_2(OH)_3CO_3$, which disappeared completely after 600 °C calcination, confirming its full decomposition.

The CuO content and impurity level of R-CuO and P-CuO are shown in Fig. 4D and E. The test results showed that the CuO contents of R-CuO (300 °C, 400 °C, 500 °C, 600 °C) were 68.48 wt%, 82.24 wt%, 94.48 wt%, and 97.90 wt% respectively, with metal impurity contents of 0.29 wt%, 0.24 wt%, 0.22 wt%, and 0.20 wt%, and chloride contents of 0.0040 wt%, 0.0020 wt%, 0.0014 wt%, and 0.0014 wt%. In contrast, the CuO contents of P-CuO (300 °C, 400 °C, 500 °C, 600 °C) were 80.24 wt%, 92.24 wt%, 98.54 wt%, and 98.80 wt% respectively, with metal impurity contents of 0.22 wt%, 0.15 wt%, 0.15 wt%, and 0.11 wt%, and chloride contents of 0.0014 wt%, 0.0013 wt%, 0.0012 wt%, and 0.0012 wt%. The experimental results demonstrated that purification treatment and calcination had a synergistic optimization effect on the preparation process of CuO. At the same calcination temperature, P-CuO exhibited higher CuO content (*e.g.*, 80.24 wt% purity at 300 °C compared to 68.48 wt% for R-CuO) and lower impurity levels (both metallic impurities and chlorides). Notably, R-CuO forms a $Cu_2Cl(OH)_3$ impurity phase at 300 °C due to residual chlorides, while this phenomenon was absent for P-CuO, confirming that purification effectively reduced chloride influence. As the calcination temperature increases (300–600 °C), the CuO content of the calcined products significantly improved and impurity levels gradually decreased. However, P-CuO maintains lower residual metallic impurities (0.11 wt% at 600 °C *vs.* 0.20 wt% for CuO–O) and chlorides (0.0012 wt% *vs.* 0.0014 wt%), demonstrating that purification treatment can synergistically enhance product purity with calcination.

The XPS spectra of R-CuO (600 °C) and P-CuO (600 °C) are shown in Fig. 5A and B, respectively. In the Cu(2p) spectra of both samples, the results revealed Cu $2p_{3/2}$ (933.5–934.5 eV) and Cu $2p_{1/2}$ (953.5–954.5 eV) peaks, confirming the presence of Cu in +2 oxidation state (Cu^{2+}) with no detectable Cu^+ or Cu^0. The C 1s spectrum of R-CuO clearly showed a C=O peak (291.5 eV), suggesting that the precursor solution may contain incompletely removed organic additives (such as complexing agents, stabilizers or surfactants) that remained on the CuO surface. The purification process (including filtration, ion exchange and centrifugation) likely effectively removed these organic impurities, as evidenced by the absence of C=O peak in P-CuO's C1s spectrum. In the O 1s spectra, R-CuO exhibited significantly higher binding energy, indicating the precursor solution may contain oxidative impurities (such as residual H_2O_2, nitrates or sulfates) that formed high-valence oxygen species during preparation. This could also result from impurity doping or increased oxygen vacancies, causing lattice distortion, thereby elevating the O 1s binding energy. Meanwhile, the purification process removed these impurities, resulting in predominantly lattice oxygen in the product and consequently lower overall O 1s binding energy for P-CuO.

The TEM images showed that R-CuO particles (Fig. 5C) were nearly spherical with mixed rod-like flake particles, having sizes of 110–120 nm and exhibiting some agglomeration, likely due to high surface energy causing aggregation through van der Waals forces or –OH interactions. In contrast, P-CuO (Fig. 5D) displayed more uniform spherical particles of about 110 nm. HRTEM images in Fig. 5C and D revealed that both products have a lattice spacing of 0.23 nm, corresponding to the (200) plane of a CuO crystal.

2.2.2.2 Calcination time. The XRD patterns of P-CuO prepared with different calcination times are shown in Fig. 6A. The main diffraction peaks of P-CuO appeared at 32.4°, 35.3°, 38.5°, 48.8°, 53.3°, 58.1°, 61.5°, 66.2°, and 67.9°, confirming the formation of highly crystalline monoclinic CuO (JCPDS no. 89-5897). With increasing calcination time, the diffraction peaks of various crystal planes in P-CuO showed no significant changes.

The SEM images in Fig. 6B demonstrated that P-CuO (2 h) exhibited particle sizes of approximately 110–130 nm with noticeable particle agglomeration. With prolonged calcination time, P-CuO (3 h) and P-CuO (4 h) showed slightly increased particle sizes and expanded interparticle gaps, along with reduced agglomeration. This phenomenon primarily resulted from extended calcination, promoting tighter particle contact, where grain boundary migration led to coalescence into single crystals.[33] Additionally, gas released during precursor decomposition created micropores at original sites, and prolonged calcination facilitates pore interconnection, forming more interparticle voids.

The FTIR spectra in Fig. 6C revealed that temperature significantly affects the –OH absorption near 3424 cm^{-1}. When the calcination time reaches 4 h, the –OH absorption peak nearly disappears, primarily due to thermal decomposition of the basic copper carbonate precursor $Cu_2(OH)_2CO_3$ during calcination, resulting in –OH group elimination. At the same time, the Cu–O

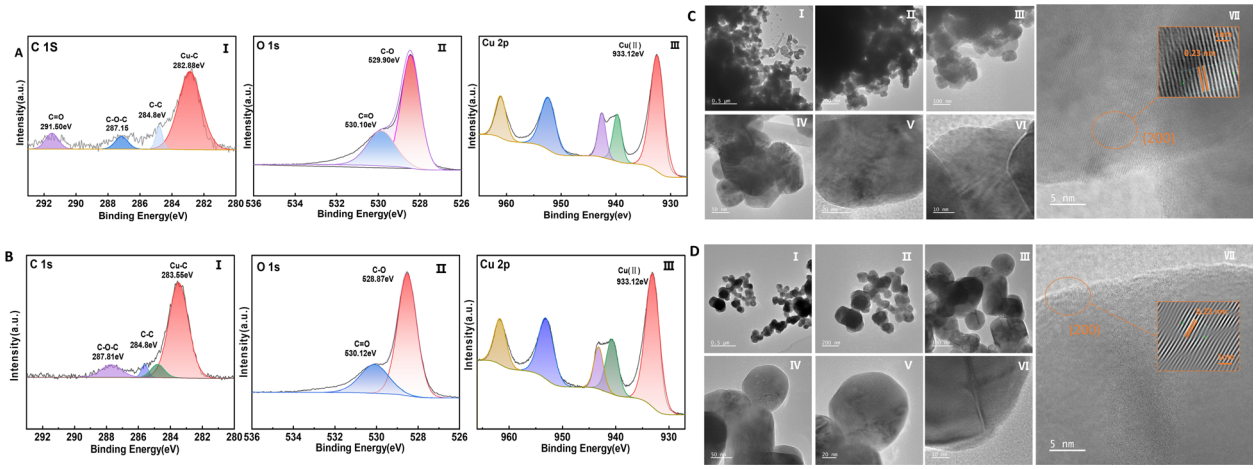

Fig. 5 XPS spectra of (A) R-CuO and (B) P-CuO. TEM images of (C) R-CuO and (D) P-CuO calcined at 600 °C.

stretching vibration peak at 530 cm^{-1} showed no significant changes.

The CuO contents and impurity contents of P-CuO prepared with different calcination durations are presented in Fig. 6D. The products calcined at 600 °C for 2 h, 3 h, and 4 h showed CuO contents of 98.98 wt%, 99.04 wt%, and 99.08 wt%, respectively, with total metal impurities below 0.12% and chloride content under 0.0015% in all cases. The results indicated that prolonged calcination time hardly altered the CuO contents of P-CuO, demonstrating complete thermal decomposition of CuO precursors (*e.g.*, $Cu_2(OH)_2CO_3$) and common impurity phases (*e.g.*, $Cu_2Cl(OH)_3$), along with thorough oxidation of intermediate crude CuO products.

2.3 Proposed transformation mechanisms

The experimental data confirmed that a Na_2CO_3/$NaHCO_3$ binary precipitant system effectively recovered high-purity $Cu_2(OH)_3CO_3$ from P-ACCEWS, with simultaneous control over the morphological aggregation state. Meanwhile, high-purity CuO nanoparticles were synthesized *via* a two-step process involving low-temperature hydrothermal conversion and subsequent calcination using $Cu_2(OH)_3CO_3$ as the precursor. The specific conversion process proceeds as follows.

2.3.1 Purification of R-ACCEWS. R-ACCEWS exhibited strong acidity, wherein copper primarily exists as Cu^{2+} and $[CuCl_4]^{2-}$ (tetrachlorocuprate(II) anion complex ions), along with organic compounds and impurity elements such as Fe, Ca,

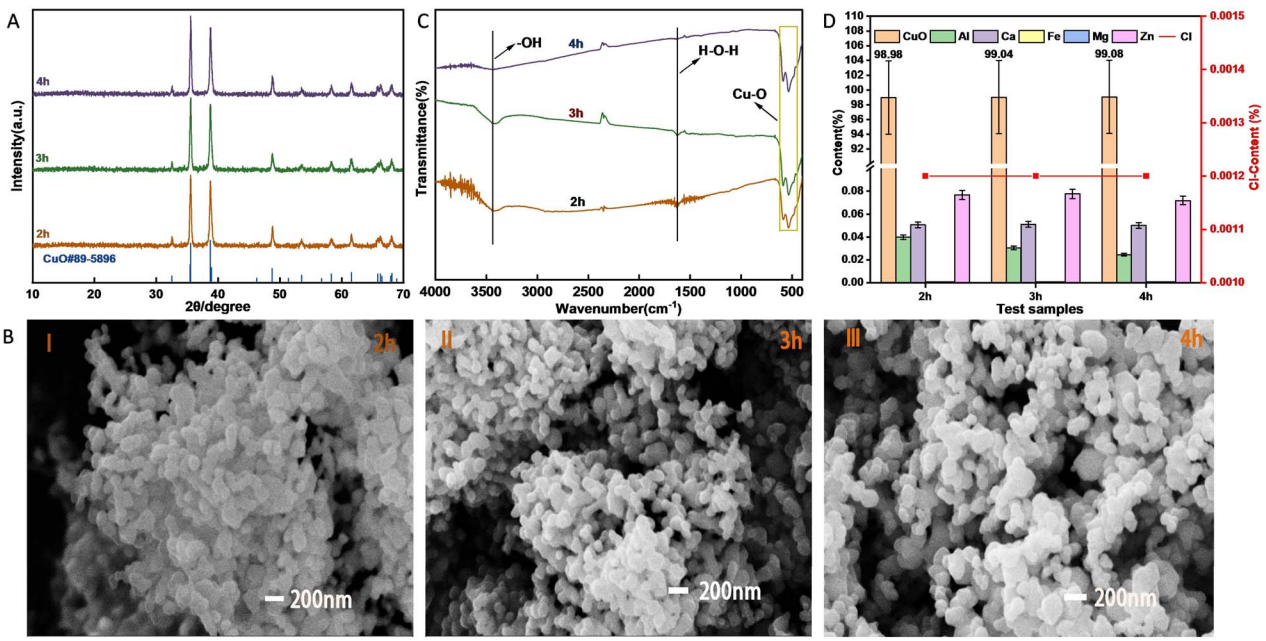

Fig. 6 (A) XRD patterns, (B) SEM images, and (C) FTIR spectra of CuO. (D) CuO contents and impurity contents of CuO calcined for different times.

Zn and so on. The pH-adjusted purification of R-ACCEWS significantly decreased acidity and metallic impurity levels in P-ACCEWS, while concurrently promoting partial hydrolysis of $[CuCl_4]^{2-}$ complexes.

2.3.2 Formation process of $Cu_2(OH)_2CO_3$. Na_2CO_3 functions as a moderately strong base that quickly raises the pH of etching waste solutions to alkaline levels (pH > 8), both providing a CO_3^{2-} source for the reaction system and effectively preventing $Cu_2(OH)_3Cl$ formation. The weaker base $NaHCO_3$ stabilized the precipitation environment *via* HCO_3^-/CO_3^{2-} equilibrium, avoiding localized pH spikes that could lead to $Cu(OH)_2$ impurity formation. In P-ACCEWS, the $Na_2CO_3/NaHCO_3$ combination created a pH 8–9 buffered system where Cu^{2+} and CO_3^{2-} progressively underwent ligand substitution and reorganization to yield soluble $[Cu(CO_3)_2]^{2-}$ (bis(carbonato)cuprate(II)). These $[Cu(CO_3)_2]^{2-}$ complexes subsequently converted to $Cu_2(OH)_2CO_3$ precursors through ligand exchange and hydrolytic condensation, eventually forming crystalline $Cu_2(OH)_2CO_3$ through combined dissolution–recrystallization and oriented assembly processes.[34–37]

2.3.3 Formation process of high-purity CuO. Under highly alkaline conditions (pH 12) at 95 °C, $Cu_2(OH)_3CO_3$ initially decomposed thermally in the hydrothermal environment to generate CuO crystal nuclei, which subsequently grew into primary CuO particles exhibiting low crystallinity and purity. During subsequent calcination at 600 °C, this crude CuO underwent three key transformations: (1) removal of organic and chlorine-containing impurities (*e.g.*, Cu(OH)Cl) through decomposition and volatilization (200–500 °C), (2) oxidation of cuprous oxide species (500–600 °C), and (3) structural reorganization, ultimately yielding high-purity nanocrystalline CuO with enhanced crystallinity.[38,39]

3. Experimental

3.1 Materials

Raw ACCEWS (R-ACCEWS): this was obtained from an environmental technology company in Mianyang, China. The solution exhibited a characteristic dark green coloration with transparency and no detectable odor, having an extremely acidic pH below 0. Inductively Coupled Plasma analysis quantified the metallic constituents as follows (mg L^{-1}): copper (97609.00), calcium (78.16), zinc (97.05), magnesium (17.31), aluminium (11.08), iron (7.86), nickel (3.62), chromium (1.90), cobalt (1.14), and manganese (0.06).

Purified ACCEWS (P-ACCEWS): a quantitative amount of R-ACCEWS was placed in a beaker with magnetic stirring at room temperature. NaOH solution and Na_2CO_3 solution of different concentrations were added to the beaker to adjust the pH of the solution to a specific value. After standing for 12 h to stabilize their pH value upon re-measurement, the solutions were filtered to obtain P-ACCEWS. The details of the purification procedure have been reported in our previous work.[40]

Other reagents: sodium hydroxide (AR, Chengdu Jinshan Chemical Reagent Co. Ltd), sodium carbonate (AR, Chengdu Kelong Chemical Reagent Factory), sodium bicarbonate (AR, Chengdu Kelong Chemical Reagent Factory), nitric acid (AR, Chengdu Kelong Chemical Co. Ltd), phosphoric acid (AR, Chengdu Jinshan Chemical Reagent Co. Ltd), sulfuric acid (AR, Chengdu Kelong Chemical Co. Ltd), potassium iodide (AR, Tianjin Beichen Fangzheng Reagent Factory), sodium thiosulfate (AR, Guangzhou Howei Pharmaceutical Technology Co. Ltd), starch indicator (Guangzhou Howei Pharmaceutical Technology Co. Ltd), silver nitrate (AR, Chengdu Kelong Chemical Co. Ltd), acetic acid (AR, Chengdu Jinshan Chemical Reagent Co. Ltd), sodium fluoride (AR, Ron Reagent), national standard reference material GSB 04-1767-2004 (Al, As, B, Ba, Be, Bi, Cd, Co, Cr, Cu, Fe, Ga, Li, Mg, Mn, Ni, Pb, Sb, Sn, Ti, V, Zn; National Analysis Center for Nonferrous Metals & Electronic Materials), national standard reference material GSB 04-1770-2004 (Cl; National Analysis Center for Nonferrous Metals & Electronic Materials), copper(II) carbonate basic reference standard (AR, Shandong Keyuan Biochemical Co. Ltd), copper(II) oxide reference standard (99%, Chengdu Jinshan Chemical Reagent Co. Ltd).

3.2 Preparation of basic copper carbonate

$Na_2CO_3/NaHCO_3$ mixture solutions (varying ratios, maintaining $\Sigma[CO_3^{2-}] = 2.4$ mol L^{-1} in 50 mL volumes) were equilibrated at a specific temperature in three-necked flasks. Then, 25 mL etching solution (either R-ACCEWS or P-ACCEWS) was dropped into the three-necked flasks with the reaction proceeding for 1.0 h at a maintained temperature. The products were immediately filtered, subjected to triple ultrasonic washing with deionized water (DI water), and oven-dried at 80 °C for 6.0 h to yield $Cu_2(OH)_2CO_3$ (R-$Cu_2(OH)_2CO_3$ or P-$Cu_2(OH)_2CO_3$).

3.3 Preparation of copper oxide

A precisely measured amount (18 mmol) of $Cu_2(OH)_2CO_3$ (either R-$Cu_2(OH)_2CO_3$ or P-$Cu_2(OH)_2CO_3$) was added into three-neck flasks with 75 mL DI water (15 : 1 liquid–solid ratio) to form a slurry. After preheating to 95 °C and adjusting the pH to 12 using 10 mol L^{-1} NaOH solution, the mixture was stirred for 120 min at 95 °C. The products were hot-filtered, ultrasonically washed 3 times with DI water, and dried at 105 °C for 2.5 h to obtain crude CuO (crude R-CuO or crude P-CuO). Final calcination at varying temperatures followed by furnace cooling produced high-purity R-CuO or P-CuO. The fabrication process is shown in Scheme 2.

3.4 Characterization

The synthesized products were systematically characterized using various analytical techniques. X-ray diffraction (XRD, TD-3700, Tongda Technology Co., China) employing Cu Kα radiation (30 kV, 20 mA) with a scanning rate of 0.1° s^{-1} across a 2θ range of 10–70° was conducted to analyze phase and crystallographic properties. Morphological features were examined using scanning electron microscopy (SEM, EVO18, Zeiss, Germany) and high-resolution transmission electron microscopy (HRTEM, JEM-F200, JEOL, Japan) operated at 200 kV. Fourier transform infrared spectroscopy (FTIR-650S, Gangdong Technology Co., China) was employed to characterize the molecular

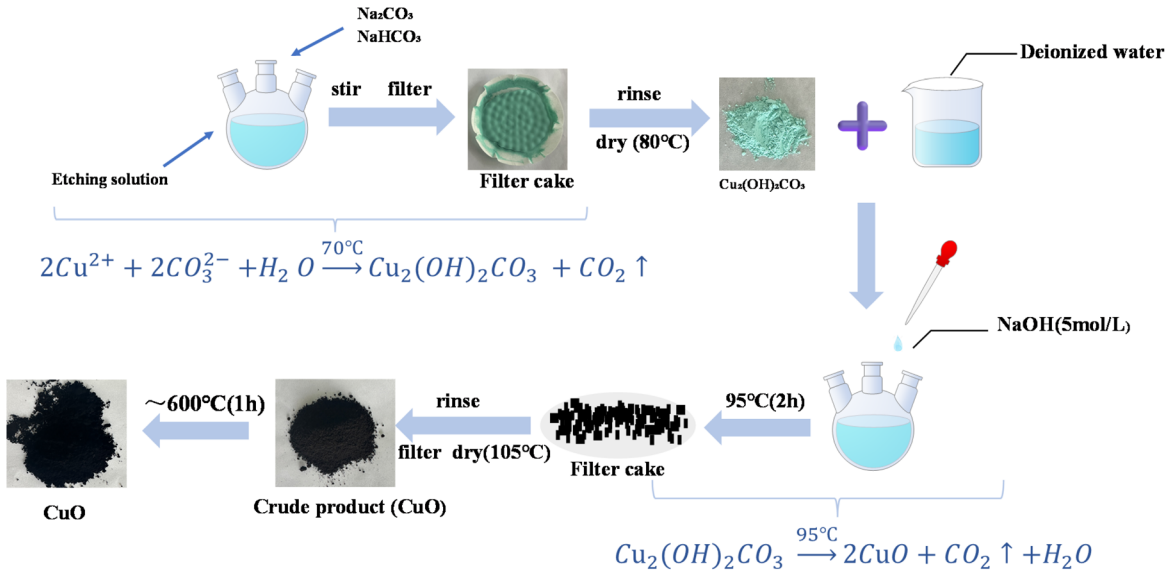

Scheme 2 Schematic illustration of the fabrication process of CuO.

structure. Thermal behavior was investigated through thermogravimetric analysis (TGA, BJ HENVEN, Hengjiu Experimental Equipment Co., China) with a controlled heating rate of 5°C min^{-1} from room temperature to 1000 °C. Surface chemical states were analyzed using X-ray photoelectron spectroscopy (XPS, ESCALAB Xi+, Thermo Scientific) under ultrahigh vacuum conditions (<5 × 10^{-9} mbar) with monochromatic Al Kα radiation (1486.68 eV), acquiring both survey (100 eV pass energy) and high-resolution (50 eV pass energy) spectra calibrated to a work function of 4.20 eV.

3.5 Testing methods for purity and impurity contents of BCC

The determination of copper content, chloride ions, and metallic impurity elements in $Cu_2(OH)_2CO_3$ was performed in accordance with the Chinese chemical industry standard HG/T4825-2015 "Industrial Basic Copper Carbonate".

3.5.1 Copper contents. A moistened sample (0.4 ± 0.0002 g) was dissolved in concentrated sulfuric acid (0.4 mL) in an iodine flask, which was diluted to 100 mL with DI water. Saturated sodium carbonate solution was dropped into the solution until slight precipitation was observed. Then, 4 mL acetic acid solution (36%), 2 mL saturated sodium fluoride solution, and 3 g potassium iodide were all added to this solution to obtain the pre-testing solution. Standardized sodium thiosulfate solution was dropped into the pre-testing solution until the solution became pale yellow. Finally, 3 mL starch indicator was added to it and continuously titrated until complete blue color disappearance persisted for 30 s as the endpoint.

$$w_1 = \frac{(V - V_0)cM \times 10^{-3}}{m} \times 100\% \quad (9)$$

where V_0 (mL) and V (mL) represent the sodium thiosulfate titrant volumes for the blank and sample titrations, respectively; c (mol L^{-1}) is the $Na_2S_2O_3$ solution molarity; and m (g) and M (g mol^{-1}) correspond to the sample mass and copper molar mass.

3.5.2 Chloride contents. 1.00 ± 0.01 g of copper(II) carbonate basic reference standard (AR, purchased from Shandong Keyuan Biochemical Co., Ltd) was dissolved in nitric acid solution in a beaker. Then, 5 mL silver nitrate solution was added to this solution and followed by diluting to 100 mL with DI water. After standing for 12–18 h, it was filtered through a sintered glass filter (pore size 5–15 μm) and the filtrate collected in a reagent bottle (denoted as Solution A). The as-prepared sample (1.00 ± 0.01 g) was dissolved in nitric acid and diluted to 100 mL to obtain Solution B.

Firstly, Solution B (10 mL) was placed into a colorimetric tube (50 mL). Then 2 mL nitric acid solution was added to Solution B and then diluted to 40 mL with DI water. Finally, silver nitrate solution (1 mL) was added to the solution and diluted to the mark (50 mL). The as-prepared solution was allowed to stand for 10 min for turbidity comparison with the standard turbidity solution, which was prepared by mixing 10 mL of solution A and 5 mL chloride standard solution.

3.5.3 Metal impurity content testing procedure for BCC. ICP-OES(Plasma3000, NCS Testing Technology Co. Ltd, China) was carried out to measure the metal impurity contents. The measured samples were prepared according to the following procedure. The as-prepared samples (0.1 g) were dissolved in HNO_3 solution, which were transferred to volumetric flasks (100 mL) and diluted to the mark with DI water. The contents were calculated using the following equation:

$$w_2 = \frac{x}{M \times \frac{10^3}{\text{mL}}} \times 100\% \quad (10)$$

where x (mg L^{-1}) denotes the concentration of metallic impurities quantified by ICP-OES and M (g) represents the mass of the analyzed sample.

3.6 Testing methods for purity and impurity contents of CuO

The determination of CuO content, chloride content, and metallic impurity content in CuO was conducted in accordance with the methods specified in the Chinese chemical industry standard HG/T 5354-2018 "Industrial Activated Copper Oxide".

3.6.1 CuO contents. An as-prepared sample (0.2 ± 0.0002 g) was firstly moistened in an iodine flask and then H_3PO_4 (5 mL) and DI water (15 mL) were poured into it. Then, sodium thiosulfate solution was titrated into the iodine flask until the solution transitioned to a light yellow. 3 mL of starch indicator solution was added to the light yellow solution, followed by continued titration with sodium thiosulfate solution until the complete disappearance of the blue coloration. The CuO contents were calculated by the following formula:

$$w_1 = \frac{(V - V_0)cM \times 10^{-3}}{m} \times 100\% \quad (11)$$

where V_0 (mL) and V (mL) denote the volumes of sodium thiosulfate solution consumed during the titration of the control sample and the as-prepared samples, respectively, c (mol L^{-1}) is the molar concentration of sodium thiosulfate solution and m (g) and M (g mol^{-1}) are the weight of as-prepared samples and molar mass of CuO, respectively.

3.6.2 Chloride contents. The as-prepared samples (10.0 ± 0.1 g) and HNO_3 solution (40 mL, 50 vol%) were added to beakers and stirred for 10 min to completely dissolve the samples. The solutions were quantitatively transferred to a volumetric flask (100 mL) and diluted to the mark with DI water, denoting as solution A. Then, 10 g of CuO (99%, AR) was dissolved in HNO_3 solution (40 mL, 50 vol%), and then 5 mL $AgNO_3$ solution (17 g L^{-1}) was added to it to form a standard mixture solution. The standard mixture was transferred to a 100 mL volumetric flask and diluted to the mark with DI water, denoting as solution B. Solution A (10 mL) and solution B (10 mL) were separately placed in two colorimetric tubes (50 mL). Then, HNO_3 solutions (2 mL, 50 vol%) were introduced to the two colorimetric tubes and diluted to 25 mL with DI water, while solution A required additional $AgNO_3$ solution (0.5 mL, 17 g L^{-1}). Subsequently, 1.5 mL of certified chlorine standard solution (GBW(E)086195) was introduced into solution B to prepare a standard turbidimetric solution containing 0.06 mg L^{-1} chlorine, corresponding to a chlorine content of 0.00015% in the final product. Finally, solution A containing $AgNO_3$ was allowed to stand for 10 minutes, after which its turbidity was quantitatively compared with that of the standard turbidimetric solution prepared from solution B. If the measured turbidity of solution A was lower than that of the standard turbidimetric solution, the chlorine content in the samples was determined to be below the 0.00015% threshold.

3.6.3 Measurement of metal impurity contents. ICP-OES was carried out to measure the metal impurity contents. The measured samples were prepared according to the following procedure. The as-prepared samples (0.1 g) were dissolved in HNO_3 solution, and the resulting solutions were individually transferred to volumetric flasks (100 mL) and diluted to the mark with DI water. The contents were calculated using the following equation:

$$w_2 = \frac{x}{M \times \frac{10^3}{\text{mL}}} \times 100\% \quad (12)$$

where x (mg L^{-1}) denotes the concentration of metallic impurities quantified by ICP-OES and M (g) represents the mass of the analyzed sample.

4. Conclusions

This paper reports the design of a dual recovery route for the purification of $Cu_2(OH)_3CO_3$ and CuO from ACCEWS, effectively improving the harmless treatment and resource utilization of PCB copper chloride etching waste.

(1) The purification process efficiently eliminated chloride ions and metallic impurities from the precursor materials, substantially enhancing the purity of both $Cu_2(OH)_2CO_3$ and CuO products. Furthermore, it modified the crystallization kinetics and particle aggregation patterns, resulting in copper compounds with distinct phase compositions and morphological characteristics.

(2) Uniform spherical $Cu_2(OH)_2CO_3$ was synthesized using purified ACCEWS as the copper source under optimized conditions: 1 : 1 Na_2CO_3/$NaHCO_3$ molar ratio, 70 °C reaction temperature, and 1 h duration. The resulting product exhibited high purity with 55.52 wt% copper content, while maintaining impurity levels below 0.24 wt% for total metals and 0.05 wt% for chloride. These specifications satisfied the Class I chloride standard (≤0.05 wt%) and Class II metal impurity standard (≤0.3 wt%) as specified in HG/T 4825-2015 for high-purity basic copper carbonate.

(3) High-purity $Cu_2(OH)_2CO_3$ was hydrothermally converted to CuO using NaOH solution under low-temperature conditions. The intermediate product contained 58.42 wt% CuO, with total metallic impurities below 0.20 wt% and chloride content under 0.0015 wt%. Subsequent calcination at 600 °C for 3 hours produced high-purity CuO, achieving 99.04 wt% purity, metallic impurities below 0.12 wt%, residual chloride content under 0.0015 wt%, and a controlled average particle size of ~110 nm.

Author contributions

Conceptualization: Dengliang He and Shishan Xue; methodology: Dengliang He; software: Song Ren; validation: Song Ren, Dengliang He and Shishan Xue; formal analysis: Song Ren, Dengliang He and Shishan Xue; investigation: Song Ren; resources: Shishan Xue; data curation: Song Ren; writing—original draft preparation: Song Ren, Dengliang He and Shishan Xue; writing—review and editing: Dengliang He, Song Ren and Shishan Xue; visualization: Song Ren; supervision: Shuxin Liu; project administration: Dengliang He and Shishan Xue; funding acquisition: Shishan Xue, Dengliang He and Shuxin Liu. All authors have read and agreed to the published version of the manuscript.

Conflicts of interest

There are no conflicts to declare.

Data availability

The data supporting this article are available from the corresponding author upon reasonable request. Data, including XRD, XPS, FT-IR, SEM, TEM, TGA, ICP-OES, are available in the article.

Acknowledgements

This work was financially supported by the Opening Project of Key Laboratory of Solid Waste Treatment and Resource Recycle, Ministry of Education (25kfgk05), Open Fund of Vanadium and Titanium Resource Comprehensive Utilization Key Laboratory of Sichuan Province (2023FTSZ02), Mianyang Teachers' College Start-up Funding (QD2021A11) and Innovation Team of Mianyang Teachers' College (CXTD2023PY06).

Notes and references

1 C. Ning, C. S. K. L. Lin, D. C. W. Hui and G. McKay, *Top. Curr. Chem.*, 2017, **375**, 43.
2 K. Shah, K. Gupta and B. Sengupta, *J. Environ. Chem. Eng.*, 2018, **6**, 2874.
3 M. Yu, X. Zeng, Q. Song, L. Liu and J. Li, *J. Cleaner Prod.*, 2016, **113**, 973.
4 S. Jung, G. Dodbiba and T. Fujita, *Resour. Process.*, 2012, **59**, 9.
5 Z. Y. Huang, F. C. Xie and Y. Ma, *J. Hazard. Mater.*, 2010, **185**, 155–161.
6 D. E. I. Giannopoulou, L. D. D. Panias, and D. I. Paspaliaris, Copper recovery from spent ammoniacal etching solutions. *Proceedings of European Metallurgical Conference (EMC)*. Germany, Hannover, June 2003.
7 F. A. N. G. Zheng, *Nonferrous Met. Soc. China*, 2008, **18**, 1258–1261.
8 A. Janin, F. Zaviska, P. Drogui, J. F. Blais and G. Mercier, *J. Hazard. Mater.*, 2009, **96**, 318–326.
9 X. Li, Y. Jia, Y. Qin, M. Zhou and J. Sun, *Chemosphere*, 2021, **278**, 130483.
10 R. M. Ramírez Zamora, R. Schouwenaars, A. Durán Moreno and G. Buitron, *Water Sci. Technol.*, 2000, **42**, 119–126.
11 T. N. H. Nguyen and M. S. Lee, *J. Ind. Eng. Chem.*, 2023, **126**, 214–223.
12 X. Liu, Q. Tan, Y. Li, Z. Xu and M. Chen, *Environ. Sci. Eng.*, 2017, **11**, 10.
13 W. Dou, X. Peng and L. Kong, *Sep. Purif. Technol.*, 2022, **285**, 120348.
14 Y. Guo, J. Zheng, X. Yan, X. Liu, W. Xu, W. Liu and Z. Lin, *Surf. Interfaces*, 2022, **31**, 101969.
15 A. R. Lima, E. J. de Arruda, C. T. de Carvalho, C. M. da Silva, M. F. Fernandes, M. F. Haiashi Kato, I. Cabrin and C. F. Andrade, *Orbital:Electron. J. Chem.*, 2015, **7**, 369.
16 S. M. Pourmortazavi, I. Kohsari and S. S. Hajimirsadeghi, *Cent. Eur. J. Chem.*, 2009, **7**, 74.
17 S. Dhyani and D. P. Kamdem, *Wood Sci. Technol.*, 2012, **46**, 1203.
18 L. Shao, K. Wu, X. Jiang, M. Shui, R. Ma, M. Lao, X. T. Lin, D. J. Wang and N. Long, *Ceram. Int.*, 2014, **40**, 3105.
19 J. R. I. Hepburn, *J. Chem. Soc.*, 1927, 2883.
20 V. Radmehr, S. M. J. Koleini, M. R. Khalesi and M. R. Tavakoli Mohammadi, *J. Inst. Eng. (India): Ser. D*, 2013, **94**, 95.
21 W. Gottfried, E. Mack and L. Witzke, Process for the preparation of basic copper carbonate, *FR Pat.*, 4659555, 1987.
22 Y. Du, L. Wang, D. Guo, Z. Ma, and L. Shen, Preparation of Basic Copper Carbonate Microspheres by Precipitation Method[C]. *2015 6th International Conference on Manufacturing Science and Engineering*. Shanghai, China, 2015, pp. 11–12.
23 R. J. Candal, A. E. Regazzoni and M. A. Blesa, *J. Mater. Chem.*, 1992, **2**, 657.
24 A. L. Luna, M. A. Valenzuela, C. Colbeau-Justin, P. Vázquez, J. L. Rodriguez, J. R. Avendaño and J. M. De la Rosa, *Appl. Catal., A*, 2016, **521**, 140–148.
25 A. Benhammada, D. Trache, S. Chelouche and A. Z. Mezroua, *Z. Anorg. Allg. Chem.*, 2021, **647**, 312–325.
26 T. Kida, T. Oka and M. Nagano, *J. Am. Ceram. Soc.*, 2007, **90**, 107.
27 M. H. Chang, H. S. Liu and C. Y. Tai, *Powder Technol.*, 2011, **207**, 378.
28 Z. H. Gan, G. Q. Yu and B. K. Tay, *J. Phys. D: Appl. Phys.*, 2003, **37**, 81.
29 S. A. A. Mansour, *J. Therm. Anal.*, 1994, **42**, 1251.
30 J. M. Rami, C. D. Patel, C. M. Patel and M. V. Patel, *Mater. Today: Proc.*, 2021, **43**, 655.
31 Z. Mirghiasi, F. Bakhtiari, E. Darezereshki and E. Esmaeilzadeh, *J. Ind. Eng. Chem.*, 2014, **20**, 113.
32 C. I. Ossai and N. Raghavan, *Nanotechnol. Rev.*, 2018, **7**, 209.
33 M. Shaw, D. Samanta, S. Bera, M. K. Mahto, M. A. S. Shaik, S. Konar, I. Mondal, D. Dhara and A. Pathak, *Inorg. Chem.*, 2022, **61**, 14568.
34 Y. Zuo, C. Zhao, A. Robador, M. Wickham and S. H. Mannan, *Acta Mater.*, 2022, **236**, 118135.
35 P. K. Healy and A. Gregson, *Inorg. Chem.*, 1978, **17**, 2969.
36 J. Sun, Y. Jia and Y. Jing, *J. Nanosci. Nanotechnol.*, 2009, **9**, 5903.
37 F. Hong and Y. X. Jiu, *Micro Nano Lett.*, 2011, **6**, 639.
38 Q. Zhang, K. Zhang and D. Xu, *Prog. Mater. Sci.*, 2014, **60**, 208.
39 Y. Xu, D. Chen and X. Jiao, *J. Phys. Chem. B*, 2005, **109**, 13561.
40 D. L. He, S. Ren, S. X. Liu and S. S. Xue, *Processes*, 2025, **13**, 2807.